CHIN. PHYS. LETT. Vol. 37, No. 9 (2020) 090301

Butterfly-Like Anisotropic Magnetoresistance and Angle-Dependent Berry Phase in a Type-Ⅱ Weyl Semimetal WP_2

Kaixuan Zhang(张凯旋)[1†], Yongping Du(杜永平)[2†], Pengdong Wang(王鹏栋)[3], Laiming Wei(魏来明)[1], Lin Li(李林)[1], Qiang Zhang(张强)[1], Wei Qin(秦维)[1], Zhiyong Lin(林志勇)[1], Bin Cheng(程斌)[1], Yifan Wang(汪逸凡)[1], Han Xu(徐晗)[1], Xiaodong Fan(范晓东)[1], Zhe Sun(孙喆)[3,5], Xiangang Wan(万贤纲)[4,5*], and Changgan Zeng(曾长淦)[1*]

[1]*International Center for Quantum Design of Functional Materials, Hefei National Laboratory for Physical Sciences at the Microscale, CAS Key Laboratory of Strongly Coupled Quantum Matter Physics, Department of Physics, and Synergetic Innovation Center of Quantum Information & Quantum Physics, University of Science and Technology of China, Hefei 230026, China*

[2]*Department of Applied Physics and Institution of Energy and Microstructure, Nanjing University of Science and Technology, Nanjing 210094, China*

[3]*National Synchrotron Radiation Laboratory, University of Science and Technology of China, Hefei 230029, China*

[4]*National Laboratory of Solid State Microstructures and Department of Physics, Nanjing University, Nanjing 210093, China*

[5]*Collaborative Innovation Center of Advanced Microstructures, Nanjing University, Nanjing 210093, China*

(Received 4 June 2020; accepted 13 July 2020; published online 1 September 2020)

The Weyl semimetal has emerged as a new topologically nontrivial phase of matter, hosting low-energy excitations of massless Weyl fermions. Here, we present a comprehensive study of a type-Ⅱ Weyl semimetal WP_2. Transport studies show a butterfly-like magnetoresistance at low temperature, reflecting the anisotropy of the electron Fermi surfaces. This four-lobed feature gradually evolves into a two-lobed variant with an increase in temperature, mainly due to the reduced relative contribution of electron Fermi surfaces compared to hole Fermi surfaces for magnetoresistance. Moreover, an angle-dependent Berry phase is also discovered, based on quantum oscillations, which is ascribed to the effective manipulation of extremal Fermi orbits by the magnetic field to feel nearby topological singularities in the momentum space. The revealed topological character and anisotropic Fermi surfaces of the WP_2 substantially enrich the physical properties of Weyl semimetals, and show great promises in terms of potential topological electronic and Fermitronic device applications.

PACS: 03.65.Vf, 72.15.−v, 75.47.−m DOI: 10.1088/0256-307X/37/9/090301

Type-Ⅱ Weyl semimetals possess highly anisotropic electronic structures, e.g., the significantly tilted Weyl cones, and anisotropic Fermi surfaces.[1,2] Such anisotropies can be exploited to produce a wide spectrum of exciting physical properties, including the anisotropic version of the chiral anomaly,[3,4] photocurrent response,[5,6] magnetoresistance (MR),[7] and plasma mirror behavior.[8,9] Recently, WP_2 was revealed to be a new, robust type-Ⅱ Weyl semimetal, having both anisotropic hole and electron Fermi surfaces.[10−13] Since MR behavior is intimately related to the topology of the Fermi surface,[14] the anisotropies of both hole and electron Fermi surfaces may collectively lead to exotic anisotropic magnetoresistance (AMR) patterns.

In general, degenerate points (such as band crossings) may exist in the momentum space of a material, which act as monopoles to create Berry fields.[15] If an electron is moving in a closed orbit near a degenerate point in the momentum space, it acquires an additional nonzero Berry phase (φ_B) as the integral of the Berry field flux, i.e., Berry curvature, from nearby monopoles.[16−20] The nonzero Berry phase has been observed in graphene,[21,22] topological insulators,[23,24] Rashba semiconductors,[20] Dirac semimetals,[25] and Weyl semimetals,[26] manifesting in relation to quantum transport effects, particularly in relation to Shubnikov-de Haas (SdH) quantum oscillations.[16,20−27] For a Weyl semimetal without inversion symmetry, in addition to the Weyl nodes (the band crossing points of valence and conductance bands), other degenerate points may also occur, ow-

Supported by the National Natural Science Foundation of China (Grant Nos. 11974324, 11804326, U1832151, and 11674296), the Strategic Priority Research Program of Chinese Academy of Sciences (Grant No. XDC07010000), the National Key Research and Development Program of China (Grant No. 2017YFA0403600), the Anhui Initiative in Quantum Information Technologies (Grant No. AHY170000), the Hefei Science Center CAS (Grant No. 2018HSC-UE014), the Jiangsu Provincial Science Foundation for Youth (Grant No. BK20170821), the National Natural Science Foundation of China for Youth (Grant No. 11804160), and the Anhui Provincial Natural Science Foundation (Grant No. 1708085MF136).

†Kaixuan Zhang and Yongping Du contributed equally to this work.

*Corresponding authors. Email: xgwan@nju.edu.cn; cgzeng@ustc.edu.cn

© 2020 Chinese Physical Society and IOP Publishing Ltd

ing to strong spin-orbit coupling. Such topological features further enrich the fascinating physics of Weyl semimetals, presenting additional possibilities for the future design of topological electronic devices.

In this work, we investigate the type-Ⅱ Weyl semimetal WP_2 in relation to electronic transport. A four-lobed butterfly-like AMR emerges at low temperatures, gradually developing into a two-lobed variant as the temperature increases, a behavior primarily ascribed to anisotropic electron Fermi surfaces. Moreover, an angle-dependent Berry phase is also observed in the quantum oscillations, which is ascribed to topological singularities in the momentum space.

High quality WP_2 single crystals were grown via the chemical vapor transport method, using iodine as the transport agent.[28] The P, WO_3 and I_2 sources were mixed and sealed in an evacuated quartz tube, and the WP_2 crystals were grown in a two-zone furnace with a temperature gradient from 1000 ℃ (source) to 900 ℃ (sink) for ten days. The stoichiometric ratio for W:P was confirmed to be 1 : 2 by means of energy-dispersive x-ray spectroscopy. Low-field transport measurements were performed on the WP_2 crystals, employing resistivity with a rotator option in a Quantum Design physical property measurement system, where the highest magnetic field measured up to 14 T. High-field transport measurements were carried out using standard ac lock-in techniques, with a He-3 cryostat and a dc-resistive magnet (∼35 T) at the High Magnetic Field Laboratory of the Chinese Academy of Sciences (CAS). In order to improve the electrical contact, Au/Ti electrodes with a thickness of 75 nm/5 nm were first deposited onto the sample by the hard-mask method, after which gold wires were employed to make contacts between the chip carrier and the Au/Ti electrodes with silver paint.

As depicted in Fig. 1(a), the WP_2 crystals, grown as described above, possess an orthorhombic structure (β-phase).[29,30] Figure 1(b) shows a high-resolution transmission electron microscopy (TEM) image and a corresponding selected area electron diffraction (SAED) pattern, which illustrate the high quality of the single crystal at the atomic scale. The crystalline long axis, i.e., the direction of growth, is the [100] direction. The biggest crystal face of the as-grown WP_2 single crystals is the (021) plane (up to 3 mm × 2 mm), confirmed by an x-ray diffraction (XRD) measurement [Fig. 1(c)] with a small full width at half maximum (FWHM) in terms of the rocking curve (∼0.05°). The powder XRD results after single crystals ground into powders are displayed in Fig. 1(d), where the perfect match of the experimental result with the calculated pattern for β-phase WP_2 further demonstrates its high crystalline quality and purity. Figure 1(e) shows a typical STM image of the cleaved (021) surface, with a terrace height of ∼0.37 nm, very close to the (021) layer spacing ∼0.371 nm.[30] The high-resolution STM image in Fig. 1(f) shows the atomic chain structure along the [100] direction, and the white rectangular region represents a unit cell of the (021) surface.

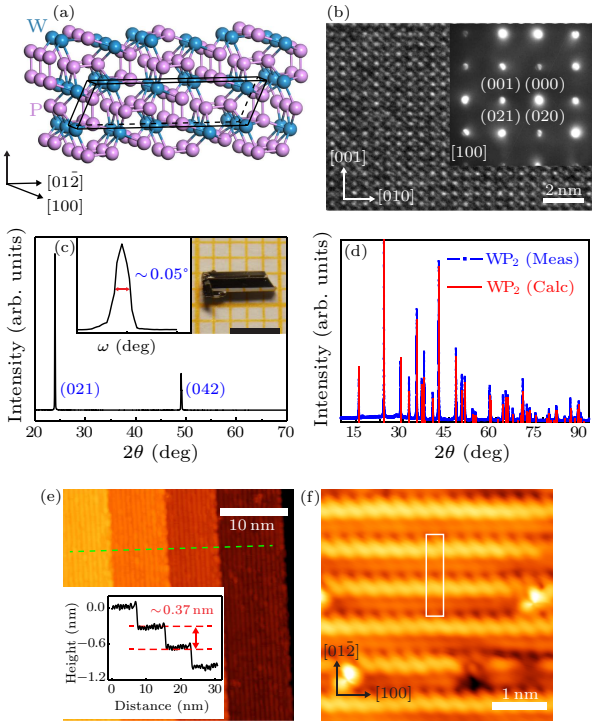

Fig. 1. Structure characterizations. (a) Crystallographic structure of WP_2 with a (021) surface. The blue and purple balls represent W and P atoms, respectively. The black lines indicate a unit cell. (b) TEM and SAED of a single WP_2 crystal. The scale bar is 2 nm. (c) Single-crystal XRD pattern of a WP_2 single crystal. The insets show the FWHM of the (021) peak in the rocking curve (∼0.05°), and the optical image of a shiny as-grown crystal. The scale bar is 3 mm. (d) Powder XRD pattern of ground WP_2 crystals. The measured peaks (blue) perfectly coincide with the calculated results (red). (e) STM image of the cleaved (021) surface with well-resolved terraces. The inset shows the height profile along the green dashed line. The scale bar is 10 nm. (f) STM image of the cleaved (021) surface with atomic resolution. The white solid rectangle denotes a surface unit cell. The scale bar is 1 nm.

The basic transport properties, including the temperature and magnetic field dependences of the WP_2's resistivity, are displayed in Fig. S1 in the Supplementary Material. Here, we focus on the interesting AMR behavior of WP_2. As illustrated in Fig. 2(a), the magnetic field B was rotated in the plane consisting of the [100] direction and the normal direction of the (021) surface, and the current I was injected along the [100] direction. The angle between B and the [100] direction is denoted as θ. As shown in Figs. 2(b) and 2(c), when B is rotated, the resistivity ρ peaks at $\theta = 60°$, 120°, 240°, and 300°, forming a butterfly-like pattern with four lobes. This is in sharp contrast to the two-lobed AMR reported previously for WP_2, with B rotating in the [100]–[010] or [010]–[001] planes.[11,31,32]

Since the electronic transport is dominated by the carriers in the vicinity of the Fermi level,[33] the MR behavior is intimately related to the topology

of the Fermi surface.[14] Theoretical calculations reveal that the Fermi surfaces of WP_2 consist of two pairs of electron and hole pockets, split by spin-orbit coupling,[9–11,31,32] as depicted in Fig. 2(d). The electron Fermi surfaces are closed, with a bow-tie-like shape, whereas the hole Fermi surfaces are open, with a spaghetti-like shape extending along the [010] direction.[11,31,32] Note that the projected electron Fermi surfaces on the rotation plane of B are also bow-tie-like, as shown in Fig. 2(e), similarly to the AMR shape. As detailed in the Supplementary Material, the butterfly-like AMR is largely determined by the intrinsic anisotropy of the electron Fermi surfaces, while both anisotropic hole and electron Fermi surfaces collectively contribute to the AMR.

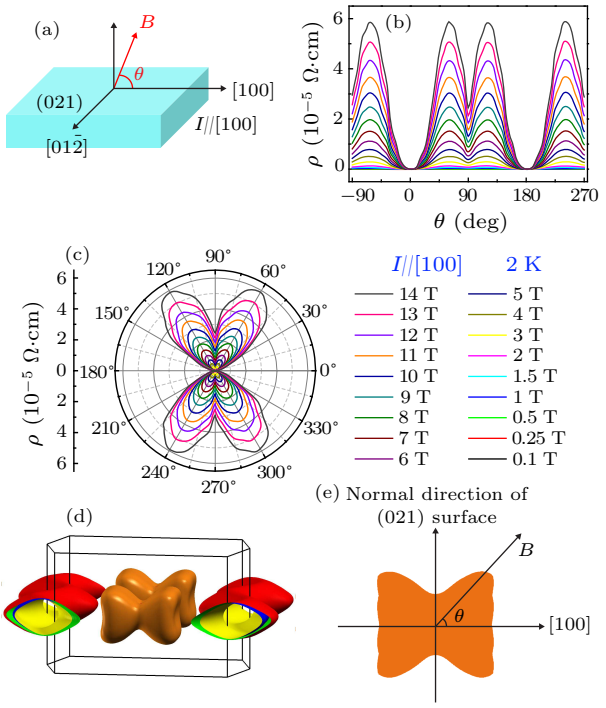

Fig. 2. Butterfly-like AMR. (a) Schematic of the measurement configuration. The current I is injected along the [100] direction. The magnetic field B is rotated in the plane consisting of the [100] direction and the normal direction of the (021) surface. The angle between the magnetic field and the [100] direction is denoted as θ. (b) Resistivity ρ as a function of θ at 2 K under various magnetic fields. (c) Polar plot of ρ as a function of θ, illustrating a butterfly-like AMR with four lobes. (d) Calculated Fermi surfaces of WP_2. The bow-tie-like closed pockets are electron Fermi surfaces, while the spaghetti-like open pockets are hole Fermi surfaces. (e) Projected electron Fermi surfaces in the rotation plane of B.

Angle-dependent magnetoresistance measurements were systemically performed under various magnetic fields and temperatures, and the results are displayed in Figs. 3(a) and S2. It is evident that when the temperature rises, the butterfly-like AMR with four lobes gradually evolves into a two-lobed AMR. To quantitatively characterize this feature, the angle where the resistivity peaks (θ_{max}) and the AMR ratio defined as $[\rho(\theta_{max}) - \rho(90°)]/\rho(\theta_{max})$ are plotted versus temperature, as shown in Fig. 3(b). We observe that θ_{max} varies from 60° to 90° with increasing temperature, whereas the AMR ratio vanishes. Such AMR evolution upon increasing temperature is primarily due to the reduced relative contribution of electron Fermi surfaces compared to hole Fermi surfaces in relation to magnetoresistance.

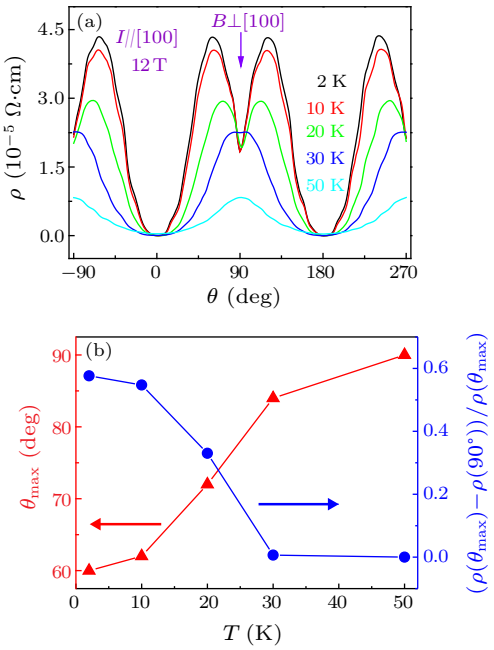

Fig. 3. Temperature-dependent evolution of the AMR. (a) Characteristics of ρ as a function of θ with $B = 12$ T at various temperatures. (b) The angle of the resistivity peak (θ_{max}) and the AMR ratio $[\rho(\theta_{max}) - \rho(90°)]/\rho(\theta_{max})$ versus T.

The exploration of the exotic effects originating from particularities, such as strong anisotropy, of the Fermi surfaces, i.e., Fermitronics, is an emerging research area in the field of electronics.[34] Here, we demonstrate that the AMR effect in WP_2 can be effectively engineered by selectively tailoring the anisotropy of the carrier trajectories at the three-dimensional Fermi surfaces by, for example, varying the direction of the applied magnetic field and temperature.

The nontrivial topological nature of Weyl semimetals is their most attractive property, and the Berry phase can be experimentally determined using phase information derived from SdH quantum oscillations.[18,22–30] Next, we exploit the Berry phase of WP_2, using quantum oscillation as an effective probe. Figure 4(a) shows the resistivity, ρ, as a function of B at various θ's, with a B value of up to 33 T. The magnetoresistance oscillations appear at high fields, and are attributed to SdH quantum oscillations.[20–27] The SdH oscillations originate from the quantization of the closed electronic orbits under an applied magnetic field, following the

Lifshitz–Onsager quantization rule,[35–37] and incorporating the Berry phase.[15,20] To better illustrate the SdH quantum oscillations, the classical nonoscillatory background is subtracted from ρ[11,31,32,34] (see more details in the Supplementary Material), and the oscillatory component $\Delta\rho$ is depicted in Fig. 4(b).

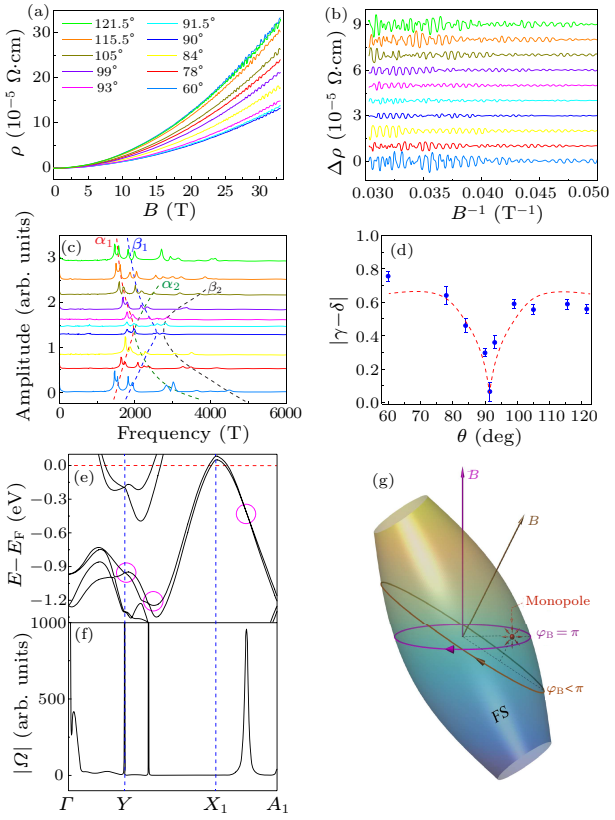

Fig. 4. Quantum oscillations. (a) Resistivity ρ as a function of B at 2 K for various θ's. (b) The oscillatory component $\Delta\rho$ as a function of $1/B$ after the subtraction of a smooth MR background from ρ. (c) FFT spectra of $\Delta\rho$ at various θ's. The dashed curves denote the calculated angular dependences of the SdH frequencies associated with the individual extremal cross-sectional orbits of the hole Fermi surface pockets (α_1, α_2, β_1, and β_2). (d) Magnitude of the total phase $|\gamma-\delta|$ as a function of θ for the α_1 branch of the hole Fermi surfaces. The red dashed curve serves as a guide to the eyes for the evolution trend of the total phase. (e) Calculated bulk band structures of WP_2 along the Γ–Y–X_1–A_1 direction. The pink circles mark the band crossing points of the two valence subbands. (f) Theoretically calculated magnitude of the Berry curvature $|\Omega|$ of the valence bands along the Γ–Y–X_1–A_1 direction. $|\Omega|$ peaks at the band crossing points. (g) Schematic of the angle-dependent Berry phase in the presence of a monopole when rotating the magnetic field.

Figure 4(c) displays the fast Fourier transform (FFT) spectra of $\Delta\rho$ at different θ's. The multiple peaks in the FFT spectra can be ascribed to different extremal cross-sectional orbits of individual hole Fermi surface pockets by comparing their frequencies with the theoretically calculated values,[31] as confirmed by the Supplementary Material. The frequencies of these peaks vary with θ, indicating the quasi-two-dimensional nature of the Fermi surface pockets.[31,32,34] Note that the FFT peak associated with the α_1 branch of the hole Fermi surfaces splits into double peaks, which may originate from fine structures beyond the calculation resolution.[38] On the other hand, no pronounced FFT peak related to the electron Fermi surfaces is observed (for further details, see the Supplementary Material).

We now focus on the Berry phase for the α_1 branch of the hole Fermi surfaces, since its FFT peaks are well resolved at all measured angles. Following the methods described in previous studies,[26,39,40] the SdH oscillation components associated with the double FFT peaks of the α_1 branch are extracted, and the corresponding total phase magnitude $|\gamma-\delta|$ is derived from the two-band Lifshitz–Kosevich fitting [see Figs. 4(d) and S3, and additional details in the Supplementary Material]. Here $\gamma = 1/2 - \varphi_B/2\pi$ is the Onsager phase, and the phase shift δ equals zero for two-dimensional (2D) or $\pm 1/8$ for three-dimensional (3D) cases.[26,39,40] We observe that $|\gamma-\delta|$ drops from $\sim$0.8 at 60° to $\sim$0.07 at 91.5° before increasing once more to $\sim$0.6 near 120°, indicating a highly tunable Berry phase. In particular, $|\gamma-\delta|$ is almost zero at 91.5°, suggesting a Berry phase close to π [a π Berry phase leads to $|\gamma-\delta| = 0$ (2D) or $|\gamma-\delta| = 1/8$ (3D)].[26,39,40]

A similar angle-dependent Berry phase has also been recently reported in ZrSiS,[34] although the underlying mechanism is unclear. In relation to this work, such behavior can be attributed to the shape of the extremal Fermi orbit, perpendicular to the applied magnetic field B and its relative position with respect to the Berry curvature monopoles. Based on our theoretical calculations, there are quite a few crossing points for the two valence subbands of WP_2, some of which, relating to the high-symmetry line, are depicted in Fig. 4(e). As shown in Fig. 4(f), the Berry curvature sharply peaks at these band crossing points, which can be theoretically regarded as monopoles, serving as the source or sink of the Berry field or Berry curvature in the momentum space.[15,17] Although the Berry curvature is generated by these monopoles, located at several hundreds of meV below the Fermi level, as marked in Fig. 4(e), the corresponding Berry connection tends to extend through entire energy bands.[27] In the presence of an external magnetic field, carriers near the Fermi surface move along the extremal cross-sectional orbit, accumulating a Berry phase equal to the path integral of the Berry connection.[16–20] When the magnetic field is rotated, the shape of the extremal cross-sectional orbit and its relative position with respect to these monopoles vary accordingly, thereby altering the path integral of the Berry connection along the orbit, i.e., the Berry phase. Fig. 4(g) depicts a simplified case with only a single monopole: when the extremal cross-sectional orbit of carriers perpendicular to B happens to en-

close the monopole, the corresponding Berry phase equals π.[16,17] While B is rotated to generate an extremal cross-sectional orbit away from the monopole, the Berry phase gradually decreases.

It is well established that the nonzero Berry phase of Fermi surfaces may induce exotic effects, e.g., the half-integer quantum Hall effect[21,22] and the valley Hall effect[41] in 2D graphene. In contrast to 2D systems, the Berry phase for carriers moving in varying closed orbits in 3D systems can effectively be tuned, as demonstrated in this work. This high tunability of the Berry phase in 3D systems paves the way to controlling interesting topological quantum effects.

In summary, electronic transport reveals a butterfly-like AMR at low temperatures, and its temperature-dependent evolution, mainly arising from anisotropic electron Fermi surfaces. Moreover, an angle-dependent Berry phase is demonstrated, based on SdH quantum oscillations, which may be attributed to topological singularities in the momentum space. Our findings not only provide a deeper insight into the topological and Fermi surface properties of Weyl semimetals, but also promise potential applications in corresponding topological electronic and Fermitronic devices.

A portion of this work was performed using the Steady High Magnetic Field Facilities, High Magnetic Field Laboratory, CAS. We thank Li Pi and Chuanying Xi for their experimental support and helpful discussions.

References

[1] Soluyanov A A, Gresch D, Wang Z, Wu Q, Troyer M, Dai X and Bernevig B A 2015 *Nature* **527** 495
[2] Deng K, Wan G, Deng P, Zhang K, Ding S, Wang E, Yan M, Huang H, Zhang H, Xu Z, Denlinger J, Fedorov A, Yang H, Duan W, Yao H, Wu Y, Fan S, Zhang H, Chen X and Zhou S 2016 *Nat. Phys.* **12** 1105
[3] Wang Y, Liu E, Liu H, Pan Y, Zhang L, Zeng J, Fu Y, Wang M, Xu K, Huang Z, Wang Z, Lu H Z, Xing D, Wang B, Wan X and Miao F 2016 *Nat. Commun.* **7** 13142
[4] Lv Y Y, Li X, Zhang B B, Deng W Y, Yao S H, Chen Y B, Zhou J, Zhang S T, Lu M H, Zhang L, Tian M, Sheng L and Chen Y F 2017 *Phys. Rev. Lett.* **118** 096603
[5] Ma J, Gu Q, Liu Y, Lai J, Yu P, Zhuo X, Liu Z, Chen J H, Feng J and Sun D 2019 *Nat. Mater.* **18** 476
[6] Wang Q, Zheng J, He Y, Cao J, Liu X, Wang M, Ma J, Lai J, Lu H, Jia S, Yan D, Shi Y, Duan J, Han J, Xiao W, Chen J H, Sun K, Yao Y and Sun D 2019 *Nat. Commun.* **10** 5736
[7] Chen D, Zhao L X, He J B, Liang H, Zhang S, Li C H, Shan L, Wang S C, Ren Z A, Ren C and Chen G F 2016 *Phys. Rev. B* **94** 174411
[8] Frenzel A J, Homes C C, Gibson Q D, Shao Y M, Post K W, Charnukha A, Cava R J and Basov D N 2017 *Phys. Rev. B* **95** 245140
[9] Zhang K, Du Y, Qi Z, Cheng B, Fan X, Wei L, Li L, Wang D, Yu G, Hu S, Sun C, Huang Z, Chu J, Wan X and Zeng C 2020 *Phys. Rev. Appl.* **13** 014058
[10] Autes G, Gresch D, Troyer M, Soluyanov A A and Yazyev O V 2016 *Phys. Rev. Lett.* **117** 066402
[11] Kumar N, Sun Y, Xu N, Manna K, Yao M, Suss V, Leermakers I, Young O, Forster T, Schmidt M, Borrmann H, Yan B, Zeitler U, Shi M, Felser C and Shekhar C 2017 *Nat. Commun.* **8** 1642
[12] Razzoli E, Zwartsenberg B, Michiardi M, Boschini F, Day R P, Elfimov I S, Denlinger J D, Süss V, Felser C and Damascelli A 2018 *Phys. Rev. B* **97** 201103(R)
[13] Yao M Y, Xu N, Wu Q S, Autes G, Kumar N, Strocov V N, Plumb N C, Radovic M, Yazyev O V, Felser C, Mesot J and Shi M 2019 *Phys. Rev. Lett.* **122** 176402
[14] Kosevich A M 2004 *Low Temp. Phys.* **30** 97
[15] Berry M V 1984 *Proc. R. Soc. London A* **392** 45
[16] Mikitik G P and Sharlai Y V 1999 *Phys. Rev. Lett.* **82** 2147
[17] Fang Z, Nagaosa N, Takahashi K S, Asamitsu A, Mathieu R, Ogasawara T, Yamada H, Kawasaki M, Tokura Y and Terakura K 2003 *Science* **302** 92
[18] Mikitik G and Sharlai Y V 2004 *Phys. Rev. Lett.* **93** 106403
[19] Yao Y, Kleinman L, MacDonald A, Sinova J, Jungwirth T, Wang D S, Wang E and Niu Q 2004 *Phys. Rev. Lett.* **92** 037204
[20] Murakawa H, Bahramy M S, Tokunaga M, Kohama Y, Bell C, Kaneko Y, Nagaosa N, Hwang H Y and Tokura Y 2013 *Science* **342** 1490
[21] Novoselov K S, Geim A K, Morozov S V, Jiang D, Katsnelson M I, Grigorieva I V, Dubonos S V and Firsov A A 2005 *Nature* **438** 197
[22] Zhang Y, Tan Y W, Stormer H L and Kim P 2005 *Nature* **438** 201
[23] Sacepe B, Oostinga J B, Li J, Ubaldini A, Couto N J, Giannini E and Morpurgo A F 2011 *Nat. Commun.* **2** 575
[24] Qu D X, Hor Y S, Xiong J, Cava R J and Ong N P 2010 *Science* **329** 821
[25] Zhao Y, Liu H, Zhang C, Wang H, Wang J, Lin Z, Xing Y, Lu H, Liu J, Wang Y, Brombosz S M, Xiao Z, Jia S, Xie X C and Wang J 2015 *Phys. Rev. X* **5** 031037
[26] Hu J, Liu J Y, Graf D, Radmanesh S M, Adams D J, Chuang A, Wang Y, Chiorescu I, Wei J, Spinu L and Mao Z Q 2016 *Sci. Rep.* **6** 18674
[27] Xiao D, Chang M C and Niu Q 2010 *Rev. Mod. Phys.* **82** 1959
[28] Mathis H, Glaum R and Gruehn R 1991 *Acta Chem. Scand.* **45** 781
[29] Rundqvist S and Lundstrom T 1963 *Acta Chem. Scand.* **17** 37
[30] Rühl R and Jeitschko W 1983 *Monatsh. Chem. - Chem. Mon.* **114** 817
[31] Schönemann R, Aryal N, Zhou Q, Chiu Y C, Chen K W, Martin T J, McCandless G T, Chan J Y, Manousakis E and Balicas L 2017 *Phys. Rev. B* **96** 121108(R)
[32] Wang A, Graf D, Liu Y, Du Q, Zheng J, Lei H and Petrovic C 2017 *Phys. Rev. B* **96** 121107(R)
[33] Ashcroft N and Mermin N 1976 *Solid State Physics* (San Diego: Harcourt College Publisher)
[34] Ali M N, Schoop L M, Garg C, Lippmann J M, Lara E, Lotsch B and Parkin S S 2016 *Sci. Adv.* **2** e1601742
[35] Onsager L 1952 *Philos. Mag.* **43** 1006
[36] Lifshitz I M and Kosevich A M 1956 *Sov. Phys.-JETP* **2** 636
[37] Lifshitz I M and Kosevich A M 1958 *Sov. Phys.-JETP* **6** 67
[38] Arnold F, Shekhar C, Wu S C, Sun Y, Dos Reis R D, Kumar N, Naumann M, Ajeesh M O, Schmidt M, Grushin A G, Bardarson J H, Baenitz M, Sokolov D, Borrmann H, Nicklas M, Felser C, Hassinger E and Yan B 2016 *Nat. Commun.* **7** 11615
[39] Li C H, Long Y J, Zhao L X, Shan L, Ren Z A, Zhao J Z, Weng H M, Dai X, Fang Z, Ren C and Chen G F 2017 *Phys. Rev. B* **95** 125417
[40] Wang Y Y, Sun L L, Xu S, Su Y and Xia T L 2018 *Phys. Rev. B* **98** 045137
[41] Gorbachev R V, Song J C W, Yu G L, Kretinin A V, Withers F, Cao Y, Mishchenko A, Grigorieva I V, Novoselov K S, Levitov L S and Geim A K 2014 *Science* **346** 448

Supplementary Material for:

Butterfly-like anisotropic magnetoresistance and angle-dependent Berry phase in Type-II Weyl semimetal WP_2 *

Kaixuan Zhang(张凯旋)[1†], Yongping Du(杜永平)[2†], Pengdong Wang(王鹏栋)[3], Laiming Wei(魏来明)[1], Lin Li(李林)[1], Qiang Zhang(张强)[1], Wei Qin(秦维)[1], Zhiyong Lin(林志勇)[1], Bin Cheng(程斌)[1], Yifan Wang(汪逸凡)[1], Han Xu(徐晗)[1], Xiaodong Fan(范晓东)[1], Zhe Sun(孙喆)[3,5], Xiangang Wan(万贤纲)[4,5**], and Changgan Zeng(曾长淦)[1**]

[1] International Center for Quantum Design of Functional Materials, Hefei National Laboratory for Physical Sciences at the Microscale, CAS Key Laboratory of Strongly Coupled Quantum Matter Physics, Department of Physics, and Synergetic Innovation Center of Quantum Information & Quantum Physics, University of Science and Technology of China, Hefei, Anhui 230026, China

[2]Department of Applied Physics and Institution of Energy and Microstructure, Nanjing University of Science and Technology, Nanjing, Jiangsu 210094, China

[3]National Synchrotron Radiation Laboratory, University of Science and Technology of China, Hefei, Anhui 230029, China

[4]National Laboratory of Solid State Microstructures and Department of Physics, Nanjing University, Nanjing, Jiangsu 210093, China

[5]Collaborative Innovation Center of Advanced Microstructures, Nanjing University, Nanjing, Jiangsu 210093, China

[†]K. Zhang, and Y. Du contributed equally to this work.

[**]Corresponding authors. Email: xgwan@nju.edu.cn; cgzeng@ustc.edu.cn

1. Electronic band structure calculations.

The electronic band structure calculations were carried out using the full potential linearized augmented plane-wave method as implemented in the WIEN2K package.[1] For topological material (TM), the band order is a key to determine the topological trivial or non-trivial bands.[2] The modified Becke-Johnson (MBJ) potential[2,3] had been used to successfully predict a wide variety of TMs.[4,5] Here, we apply the MBJ potential together with the local-density

approximation for the correlation potential (MBJLDA) to get the accurate band order and the band inversion strength.[3] The plane-wave cutoff parameter $R_{MT}K_{max}$ was set to be 7 and a 24× 24× 15 mesh was used for the BZ integral. The spin-orbit coupling was treated using the second-order variational procedure. The Fermi surfaces were generated via a more refined k-point mesh of 40 × 40 × 24. Fermi surface sheets were visualized using the XCrysden software.[6] The angular dependence of the quantum oscillatory frequencies was calculated through the Skeaf code.[7] The Berry curvature were then calculated within the tight-binding model using the WannierTools software package.[8,9] The hopping parameters were determined from the maximally localized Wannier functions,[10] which were projected from the Bloch state derived from the first-principles calculations.

2. **Temperature and magnetic field dependences of the WP_2 resistivity.**

Figure S1(a) displays the resistivity (ρ) of WP_2 as a function of temperature (T) at various magnetic fields (B), and Figure S1(b) depicts ρ as a function of B at various temperatures. The magnetic field is perpendicular to the (021) surface. An extremely low residual resistivity (~ 4 nΩ·cm at 0 T and 2 K) and a gigantic magnetoresistance (MR) (~ 10^6% at 14 T and 2 K) are revealed, comparable to the values reported recently for WP_2.[11-13] Such low residual resistivity and gigantic MR can be attributed to the topologically suppressed carrier scattering and perfect electron-hole compensation in WP_2.[13]

3. **Anisotropic magnetoresistance (AMR) arising from the anisotropy of the Fermi surface.**

As depicted in Fig. 2(a) in the main text, the magnetic field B was rotated in the plane consisting of the [100] direction and the normal direction of the (021) surface, and the current

was injected along the [100] direction. The angle between *B* and the [100] direction is denoted as θ. It is noted that the rotation of *B* is almost in the bisector plane between the [100]-[010] plane and [100]-[001] plane, and thus can be decomposed into a rotation in the [100]-[010] plane and a rotation in the [100]-[001] plane.

For the open hole Fermi surface, when *B* is rotated in the [100]-[010] plane, the MR is expected to be extremely large along the [010] direction because the anisotropic hole Fermi surface extends along such direction,[11] leading to a strong AMR with two lobes at $\theta = 90^\circ$ and 270°. In contrast, when *B* is rotated in the [100]-[001] plane, the MR is much weaker and can be neglected because the perpendicular cross-section area of the Fermi surface always remains infinite.[13] Therefore, the MR arising from the anisotropic hole Fermi surface is dominated by the MR in the [100]-[010] plane, forming a global AMR with two lobes and thus cannot account for the observed butterfly-like AMR with four lobes.

On the other hand, two body diagonals of the electron Fermi surfaces are almost in the rotation plane of *B*, therefore the projected electron Fermi surfaces on this plane are also bow-tie-like as shown in Fig. 2(e) in the main text, similar to the AMR shape. When *B* is perpendicular to the steep regions of the electron FS, the averaged cyclotron mass and cyclotron frequency of carriers travelling in the plane perpendicular to *H* are expected to be minimal and maximal,[14-17] leading to a large MR. That is, the anisotropy of the electron Fermi surfaces is expected to give rise to a butterfly-like AMR with four MR peaks along the lobes of the electron Fermi surfaces (i.e., $\theta = 45^\circ$, 135°, 225°, and 315°).[14-17] These angles are slightly deviated from the experimental observations, mainly due to the additional contributions from the anisotropic hole Fermi surfaces.

In summary, while both the anisotropic hole and electron Fermi surfaces collectively

contribute to the AMR, the observed butterfly-like four-lobe feature of AMR is largely determined by the electron Fermi surface.

4. **Analysis of the Shubnikov-de Haas (SdH) oscillations.**

To better illustrate the SdH quantum oscillations, after fitting $\rho(B)$ with a power law formula $A \times B^n$ (where A is a constant and the power n = 1.8-2.0 for different angles), the classical nonoscillatory background $A \times B^n$ is subtracted from ρ,[11-13,18] and the oscillatory component ($\Delta\rho$) is depicted in Fig. 4(b) in the main text.

Table S1 lists the theoretically calculated SdH frequencies corresponding to different extremal cross-sectional orbits of the electron and hole Fermi surfaces at various θs. Comparing these frequencies with the positions of peaks in the fast Fourier transform (FFT) spectra (Fig. 4(c) in the main text), the multiple FFT peaks can be ascribed to individual Fermi surface pockets. For example, the split double peaks at 1740 and 1870 T for $\theta = 84^\circ$ are attributed to an extremal cross-sectional orbit (α_1) of the hole Fermi surface pocket (α), whereas the peaks at 2180, 2270, and 3060 T are associated with other extremal cross-sectional orbits (α_2, β_1, and β_2) of the hole Fermi surface pockets (α and β). The α_1 peak also splits into double peaks at other θs. Similar splitting was also observed previously in WP_2[11] and TaP,[19] and are attributed to the fine structures in the hole pocket beyond the calculation resolution.[19] It is also noted that the calculated SdH frequencies of α_2 and α_1 branches merge with each other at 90˚. Nevertheless, the SdH oscillation component of the α_1 branch overwhelms that of the α_2 branch at 90˚, since the FFT amplitude of the α_2 peak is much smaller than that of the α_1 peak when θ is approaching to 90˚.

On the other hand, no pronounced peak related to the electron Fermi surfaces is observed in the FFT spectra. Therefore, the SdH oscillations are dominated by the hole Fermi surfaces,

whereas the butterfly-like AMR is largely determined by the electron Fermi surfaces as discussed earlier. The quantum mobility may be lower and the corresponding Landau level broadening of electrons may be wider than that of holes, rendering the quantization of the extremal orbits around the electron Fermi surface pockets much more difficult. Hereafter we focus on the Berry phase for the hole branches.

The Berry phase (ϕ_B) can be extracted from the SdH oscillations by the Lifshitz-Kosevich fitting[18,20,21] or the Landau level index plot.[22] However, the latter is no longer a reliable method to analyze the Berry phase for multiband electronic systems,[20,23] therefore we adopt the former method following previous studies.[20,21]

The SdH oscillation component associated with the α_1 branch of the hole Fermi surfaces is extracted using the frequency filtering and inverse FFT method.[18,24,25] The results are shown in Fig. S3. We employ the two-band Lifshitz-Kosevich formula $\Delta\rho \propto e^{\frac{-\pi}{\mu_q B}} \frac{\lambda}{\sinh(\lambda)} \left\{\cos\left[2\pi\left(\frac{B_{F1}}{B} - \delta + \gamma + \cos 2\pi B F 2 B - \delta + \gamma\right.\right.\right.$ to extract the magnitude of the total phase ($\gamma - \delta = |1/2 - \phi B/2\pi - \delta|$) related to the α_1 branch.[20] Here B_{F1} and B_{F2} are the SdH frequencies corresponding to the double FFT peaks, γ is the Onsager phase, δ is a phase shift, μ_q is the hole quantum mobility, $\lambda = \frac{2\pi^2 m^* k_b T}{\hbar e B}$, m^* is the effective mass of the α_1 holes, and k_b is the Boltzmann constant. From the temperature dependence of the SdH amplitude (data not shown), m^* is estimated to be 1.4 m_0 (m_0 is the electron rest mass), comparable to previous results of WP_2.[11]

Supplementary references

[1] Blaha P, Schwarz K, Madsen G, Kvasnicka D and Luitz J *An Augmented Plane Wave + Local Orbitals Program for Calculating Crystal Properties* (Technische Universität Wien, Wien, 2001)

[2] Feng W, Xiao D, Zhang Y and Yao Y 2010 *Phys. Rev. B* **82** 235121

[3] Tran F and Blaha P 2009 *Phys. Rev. Lett.* **102** 226401

[4] Agapito L A, Kioussis N, Goddard III W A and Ong N P 2013 *Phys. Rev. Lett.* **110** 176401

[5] Wang Z, Vergniory M G, Kushwaha S, Hirschberger M, Chulkov E V, Ernst A, Ong N P, Cava R J and Bernevig B A 2016 *Phys. Rev. Lett.* **117** 236401

[6] Kokalj A 1999 *J. Mol. Graphics Modell.* **17** 176-179

[7] Rourke P M C and Julian S R 2012 *Comput. Phys. Commun.* **183** 324-332

[8] Wu Q, Zhang S, Song H-F, Troyer M and Soluyanov A A 2018 *Comput. Phys. Commun.* **224** 405

[9] Lopez Sancho M P, Lopez Sancho J M and Rubio J 1985 *J. Phys. F* **15** 851

[10] Marzari N, Mostofi A A, Yates J R, Souza I and Vanderbilt D 2012 *Rev. Mod. Phys.* **84** 1419

[11] Schönemann R, Aryal N, Zhou Q, Chiu Y C, Chen K W, Martin T J, McCandless G T, Chan J Y, Manousakis E and Balicas L 2017 *Phys. Rev. B* **96** 121108(R)

[12] Wang A, Graf D, Liu Y, Du Q, Zheng J, Lei H and Petrovic C 2017 *Phys. Rev. B* **96** 121107(R)

[13] Kumar N, Sun Y, Xu N, Manna K, Yao M, Suss V, Leermakers I, Young O, Forster T, Schmidt M, Borrmann H, Yan B, Zeitler U, Shi M, Felser C and Shekhar C 2017 *Nat. Commun.* **8** 1642

[14] Kosevich A M 2004 *Low Temp. Phys.* **30** 97-117

[15] Yue Z J, Zhu C B, Dou S X and Wang X L 2012 *Phys. Rev. B* **86** 195120

[16] Zhu Z, Collaudin A, Fauqué B, Kang W and Behnia K 2011 *Nat. Phys.* **8** 89-94

[17] Collaudin A, Fauqué B, Fuseya Y, Kang W and Behnia K 2015 *Phys. Rev. X* **5** 021022

[18] Ali M N, Schoop L M, Garg C, Lippmann J M, Lara E, Lotsch B and Parkin S S 2016 *Sci. Adv.* **2** e1601742

[19] Arnold F, Shekhar C, Wu S C, Sun Y, Dos Reis R D, Kumar N, Naumann M, Ajeesh M O, Schmidt M, Grushin A G, Bardarson J H, Baenitz M, Sokolov D, Borrmann H, Nicklas M, Felser C, Hassinger E and Yan B 2016 *Nat. Commun.* **7** 11615

[20] Li C-H, Long Y-J, Zhao L-X, Shan L, Ren Z-A, Zhao J-Z, Weng H-M, Dai X, Fang Z, Ren C and Chen G-F 2017 *Phys. Rev. B* **95** 125417

[21] Hu J, Liu J Y, Graf D, Radmanesh S M, Adams D J, Chuang A, Wang Y, Chiorescu I, Wei J, Spinu L and Mao Z Q 2016 *Sci. Rep.* **6** 18674

[22] Murakawa H, Bahramy M S, Tokunaga M, Kohama Y, Bell C, Kaneko Y, Nagaosa N, Hwang H Y and Tokura Y 2013 *Science* **342** 1490-1493

[23] Taskin A A and Ando Y 2011 *Phys. Rev. B* **84** 035301

[24] Shen B, Deng X, Kotliar G and Ni N 2016 *Phys. Rev. B* **93** 195119

[25] Li G, Xiang Z, Yu F, Asaba T, Lawson B, Cai P, Tinsman C, Berkley A, Wolgast S, Eo Y S, Kim D J, Kurdak C, Allen J W, Sun K, Chen X H, Wang Y Y, Fisk Z and Li L 2014 *Science* **346** 1208-1212

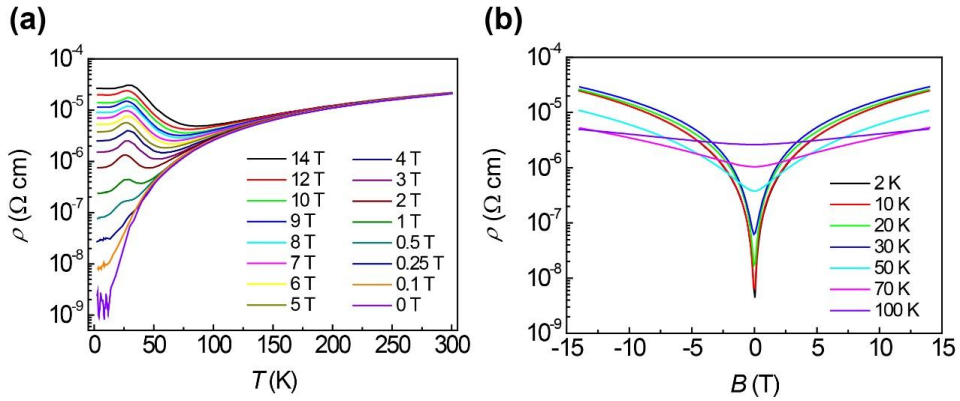

Fig. S1. Transport properties of WP_2. (a) Resistivity ρ as a function of temperature T at different magnetic fields. (b) ρ as a function of magnetic field B at various temperatures. The magnetic field in (a) and (b) is perpendicular to the (021) plane.

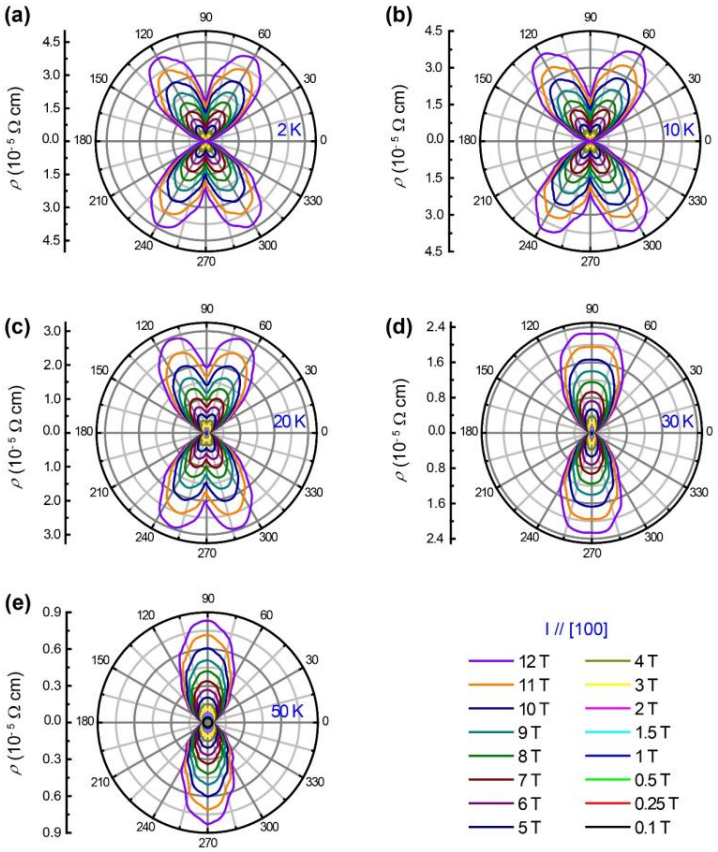

Fig. S2. Temperature-dependent evolution of the AMR. (a-e) Polar plots of ρ as a function of θ with different magnetic fields at 2 K, 10 K, 20 K, 30 K, and 50 K, respectively.

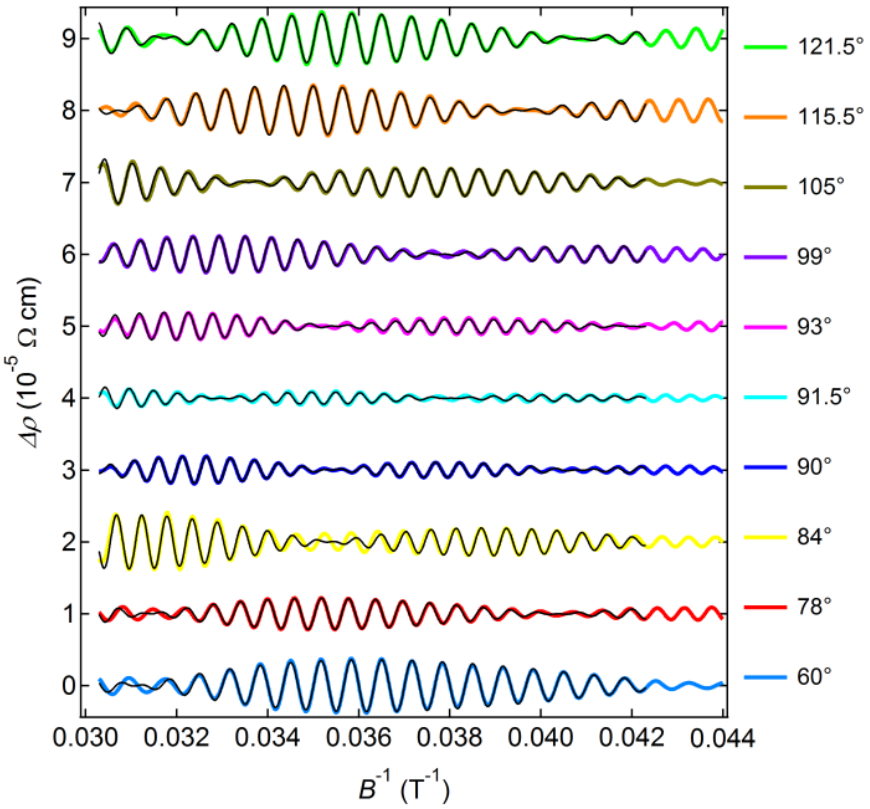

Fig. S3. SdH oscillation component of the α_1 branch of the hole Fermi surfaces at various θs. The curves are shifted vertically for clarity. The black curves are the fitting curves based on the Lifshitz-Kosevich model.

Table S1. Theoretically calculated SdH frequencies associated with individual extremal cross-sectional orbits of the hole ($F_{\alpha1}$, $F_{\alpha2}$, $F_{\beta1}$ and $F_{\beta2}$) and electron (F_{δ} and F_{γ}) Fermi surfaces at various θs.

Orbits / Angles	α_1	α_2	β_1	β_2	δ	γ
	$F_{\alpha1}$(kT)	$F_{\alpha2}$(kT)	$F_{\beta1}$(kT)	$F_{\beta2}$(kT)	F_{δ}(kT)	F_{γ}(kT)
121.5˚	1.5864	3.1768	1.9416	4.4489	4.5209	3.6235
115.5˚	1.6048	2.9061	1.9686	4.1977	4.6627	3.6167
105˚	1.6980	2.5373	2.1058	3.5893	4.7736	3.6171
99˚	1.7926	2.3161	2.2491	3.1764	4.8249	3.6471
93˚	1.9253	2.1016	2.4599	2.7657	4.8583	3.6726
91.5˚	1.9638	2.0533	2.5262	2.7376	4.8634	3.6772
90˚	1.9913	2.0027	2.5966	2.7263	4.8614	3.6736
84˚	1.8513	2.2025	2.3424	2.9582	4.8430	3.6590
78˚	1.7387	2.4252	2.1680	3.3865	4.7969	3.6276
60˚	1.5863	3.0975	1.9428	4.3931	4.5639	3.6227